

Modulation of Field-Effect Passivation at the Back Electrode Interface Enabling Efficient Kesterite-Type $\text{Cu}_2\text{ZnSn}(\text{S,Se})_4$ Thin-Film Solar Cells

Yanping Song, Huanhuan Sun, Bin Yao,* Yongfeng Li,* Zhanhui Ding, Wei Qin, Zhenzhong Zhang, Ligong Zhang, Haifeng Zhao, and Daocheng Pan

Cite This: *ACS Appl. Mater. Interfaces* 2020, 12, 38163–38174

Read Online

ACCESS |

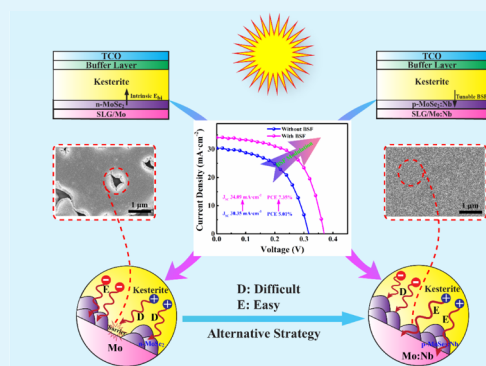
Metrics & More

Article Recommendations

Supporting Information

ABSTRACT: For further efficiency improvement in kesterite-type $\text{Cu}_2\text{ZnSn}(\text{S,Se})_4$ (CZTSSe) solar cells, it is essential to address the carrier recombination issue at the back electrode interface (BEI) caused by the undesirable built-in potential orientation toward an absorber as an $n\text{-MoSe}_2$ interfacial layer formed. In this regard, back surface field (BSF) incorporation, i.e., field-effect passivation, shows promise for dealing with this issue due to its positive effect in decreasing recombination at the BEI. In this study, the BSF was realized with the p-type conduction transition in interfacial layer MoSe_2 by incorporating Nb into the back electrode. The BSF width can be tuned via modulating the carrier concentration of the absorber, which has been demonstrated by capacitance–voltage characterization. A beyond 7% efficiency BSF-applied CZTSSe solar cell is prepared, and the effects of a tunable BSF and the mechanism underpinning device performance improvement have been investigated in detail. The wider BSF distribution in the absorber induces a decrease in reverse saturation current density (J_0) due to the stronger BSF effect in suppressing BEI recombination. As a result, an accompanying increase in open-circuit voltage (V_{OC}) and short-circuit current density (J_{SC}) is achieved as compared to the BSF-free case. This study offers an alternative strategy to address the BEI recombination issue and also broadens the interface passivation research scope of potentially competitive kesterite solar cells.

KEYWORDS: $\text{Cu}_2\text{ZnSn}(\text{S,Se})_4$ solar cells, carrier recombination, back surface field, field-effect passivation, reverse saturation current density, open-circuit voltage, short-circuit current density



1. INTRODUCTION

Kesterite-type $\text{Cu}_2\text{ZnSn}(\text{S,Se})_4$ (CZTSSe) material involving readily available and low-toxicity compositions had been emerging as a competitive candidate for CdTe and its counterpart $\text{Cu}(\text{In,Ga})\text{Se}_2$ (CIGS) absorbers; also, it possesses favorable optoelectronic properties similar to those of CIGS.^{1–6} In 2014, a power conversion efficiency (PCE) of 12.6% was achieved by the IBM group in the CZTSSe-based solar cell field.⁵ Most recently, this record PCE has broken to 12.62% by Kim et al.⁷ However, there still exists a considerable performance gap as compared to the CIGS solar cell,⁸ which is basically due to the large open-circuit voltage (V_{OC}) deficit. The V_{OC} deficit is primarily originated from the electrostatic potential fluctuations caused by antisite defect pairs Cu_{Zn} (Zn_{Cu}), nonuniform distributions of S or Se,^{9–11} and contact losses of nonmatched band alignments in interfaces involving band gap (E_{g}) offset and mismatch in work function.^{12,13}

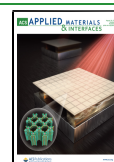
For further PCE improvement, the V_{OC} issue in CZTSSe solar cells needs to be addressed. Over the past several years, a lot of strategies were attempted. Lee et al.¹⁴ and Liu et al.¹⁵

reported that V_{OC} can be improved by introducing Al_2O_3 thin films into CZTSSe/CdS and Mo/CZTSSe interfaces because of defect passivation, respectively. Interfacial defect passivation using another ultrathin layer with high resistivity has also been investigated, such as TiN, ZnO, TiB_2 , etc.^{16–20} Additionally, Wu et al.²¹ proved a significant improvement in V_{OC} and PCE for CZTSSe solar cells by incorporating appropriate Ag into the absorber to suppress Cu_{Zn} antisite defects. Kim et al.⁶ performed a study on CZTSSe solar cells via imposing double emitters $\text{In}_2\text{S}_3/\text{CdS}$ and demonstrated a considerable increase in carrier densities after *In* incorporation, ultimately giving rise to an increase in V_{OC} .

Received: June 10, 2020

Accepted: July 30, 2020

Published: July 30, 2020



Indeed, the aforementioned strategies are of vital importance to the V_{OC} improvement and the progress of CZTSSe solar cells. As far as the V_{OC} issue is concerned, on no account can we ignore the critical function of the back surface field (BSF) that has been commonly applied in Si-based and CIGS-based solar cells.^{22–24} The BSF can bring about a positive effect in suppressing the carrier recombination at the back electrode interface (BEI) and thus result in V_{OC} improvement.^{25–27} However, there are relatively few studies devoted to the implementation of the BSF in CZTSSe solar cells except for some numerical modeling studies using Solar Cell Capacitance Simulator (SCAPS) software.^{28,29} The mainspring to highlight the BSF significance is that a barrier of photoinduced hole transportation to the back electrode exists in the BEI region due to the formation of an n-MoSe₂ interfacial layer.^{30,31} Severe carrier recombination generally occurs in the BEI region.¹² Accordingly, bringing down the hole transportation barrier really matters. One approach is to realize the conduction type transition in interfacial layer MoSe₂ and form the BSF, thereby facilitating carrier transportation. In previous work, p-type transition was fulfilled in interfacial layer MoSe₂ via incorporating Nb into the back electrode.³² Furthermore, the Fermi level of p-MoSe₂:Nb has downshifted compared with n-MoSe₂, especially that is situated lower than that of the absorber.

In this work, we investigate the BSF effect in depth. The aim is to study the impact of the BSF width distribution in the absorber on device performances. It is well known that the depletion layer width distribution of the p–n junction gets enlarged with decreasing the corresponding carrier concentration. Then, the BSF width distribution in the absorber can be tuned via modulating the carrier concentration between p-MoSe₂:Nb and p-CZTSSe, which has been demonstrated by capacitance–voltage (C–V) characterization. The wider BSF creates stronger field-effect passivation to drive holes and electrons toward back and front electrodes, respectively, hence decreasing BEI recombination and improving device performance. Besides, we also observe that p-MoSe₂:Nb comprises a compact surface without void morphology, while that for n-MoSe₂ consists of polyporous morphology. These undesirable voids can act as spatial barriers, penalizing sodium diffusion from a soda-lime glass (SLG) substrate into an absorber and mitigating the grain growth;¹⁵ also, it would aggravate the shunting problem. Therefore, the shunt resistance (R_{sh}) of the device is anticipated to be increased in BSF-applied cells as compared to the BSF-free case. Our results reveal that the V_{OC} and short-circuit current density (J_{SC}) have effectively increased by adjusting the BSF width distribution in the absorber. With the incorporation of the BSF, the corresponding PCE increases from 5.01% to above 7%, and the best efficiency of 7.35% has been achieved with promising perspectives for further improvement. This work provides a potential and viable route to interface recombination tuning and to the V_{OC} and J_{SC} improvement for prospectively efficient kesterite solar cells.

2. EXPERIMENTAL SECTION

2.1. Fabrication of Mo (Mo:Nb) Electrodes. Mo (Mo:Nb) electrodes were grown on an SLG substrate by magnetron sputtering with a direct current (DC) power of 150 W. To stabilize the adhesion between the SLG substrate and a thin film, after the well-accepted rinse process using acetone, ethanol, and deionized water sequentially, the SLG substrate was further dipped in boiled hydrogen peroxide for

30 min. This treatment can effectively wipe off the residual organic dirt and then improve the surface cleanliness of the SLG substrate. To fabricate the Nb-doped Mo electrode, a small Nb sheet with an area of 25 mm² was placed on the surface of the target. The Nb concentration in Mo:Nb was determined to be 8.96 atom % via EDS, as shown in Figure S1 (Supporting Information). The composition information of MoSe₂ and MoSe₂:Nb films is listed in Table S1 (Supporting Information).³² Differing from the common bilayer structure, the back electrode configuration was fabricated with an improved stack order of Mo-H/Mo-L/Mo-H or Mo:Nb-H/Mo:Nb-L/Mo:Nb-H (H and L represent the film sputtered at 1.8 and 0.2 Pa pressures, respectively). An additional top Mo-H or Mo:Nb-H layer can play the role of buffer in preventing overselenization to some degree.

2.2. Fabrication of the Cu₂ZnSnS₄ (CZTS) Precursor Solution and the Absorber. The absorber was prepared by a dimethyl sulfoxide (DMSO)-based solution method. First, Cu(CH₃COO)₂·H₂O and SnCl₂·2H₂O were magnetically stirred and dissolved with 10 mL of DMSO for 120 min. To make the mixed solution rapidly and fully dissolved, it was stirred at a temperature of 50 °C for the first 10 min and then at room temperature for the next 110 min. Thus, a light green and pellucid solution was obtained. After that, we added ZnCl₂ and CS(NH₂)₂ successively and continuously stirred for 120 min at room temperature. Then, a clear, transparent, and yellowish CZTS precursor solution was obtained. It is worthwhile mentioning that an appropriate amount of ethanalamine (HOCH₂CH₂NH₂) was added to improve the viscosity and reactivity of the precursor solution before spin coating and then adjust and enhance the precursor solution adhesion. The possible cracks can be avoided during spin coating. The Cu/(Zn + Sn) was controlled to be 0.72, 0.76, 0.80, and 0.84 (marked as CZTS-1, CZTS-#, CZTS-2, and CZTS-3), respectively, and keeping the Zn/Sn and S/(Cu + Zn + Sn) ratios constant for all samples. The corresponding selenized CZTSSe films were named CZTSSe-1, CZTSSe-#, CZTSSe-2, and CZTSSe-3, and the detailed information is listed in Tables S2 and S3 (Supporting Information). Second, CZTS precursor films with bilayer configuration were fabricated. The bottom and top absorbers were added successively onto Mo (Mo:Nb)-coated SLG (SLG/Mo, SLG/Mo:Nb) substrates and spin-coated with 3 and 7 layers, respectively. The roast temperature and time were 300 °C and 3 min, respectively. Then, five selenized absorbers (Table 2) were obtained by postselenization (552 °C for 15 min) under atmospheres with the flow of high-purity nitrogen and selenium vapor.

2.3. Fabrication of CZTSSe Solar Cells. To obtain the different BSF width distribution, the carrier concentration of the bottom absorber was tuned from 1.16×10^{16} to 5.35×10^{17} cm⁻³ via adjusting the Cu/(Zn + Sn), simultaneously, the carrier concentration of p-MoSe₂:Nb remains unchanged to the previous work.³² After the synthesis of the absorber, buffer layer CdS (50 nm) was grown rapidly on the absorber surface via the chemical bath deposition (CBD) method. The sources of Cd and S are derived from CdSO₄·8/3H₂O (0.04 mol L⁻¹) and CS(NH₂)₂ (0.1 mol L⁻¹), respectively. During the CBD process, we also introduced an appropriate amount of NH₄Cl (0.04 mol L⁻¹) as a buffering agent and controlled the deposition temperature and time to 75 °C and 14 min, respectively. Notably, CZTSSe films were dipped into ammonium hydroxide (NH₃·H₂O, 25.0–28.0%, Analytical Reagent) and stirred (300 rpm) for 2 min to wipe off the surface dirt before the CBD process. Subsequently, window layers containing 50 nm thick i-ZnO (60 W, 1.0 Pa, 5 min) and 260 nm thick indium tin oxide (ITO) (70 W, 0.39 Pa, 10 min) films were grown in turn on the buffer layer surface using radio frequency (RF) magnetron sputtering. Presputtering for 5 min was adopted before formal sputtering, and subsequent vacuum extraction for 20 min was also applied to discharge the residual heat after formal sputtering. In the end, 600 nm thick Ag electrodes were sequentially deposited on the ITO surface using thermal evaporation with a customized mask plate, and no antireflection layer was employed in this work. After mechanical scribing, we obtained 9 cells of 0.19 cm² upon the 2 × 2 cm² SLG substrate.

2.4. Characterization. The structural properties were analyzed by the X-ray diffraction method (XRD) carried out using a DX-2700 X-

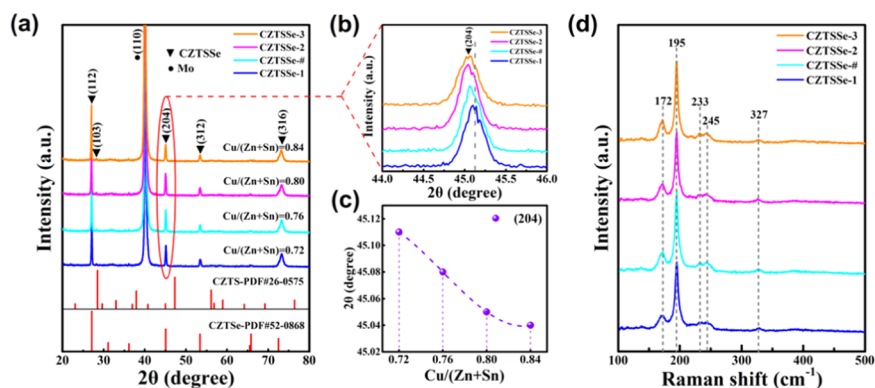


Figure 1. (a) XRD patterns, (b, c) enlarged view of (204) diffraction peaks and the corresponding diffraction angle variation, and (d) Raman spectra with a 473 nm excitation source for CZTSSe films with different Cu/(Zn + Sn), respectively.

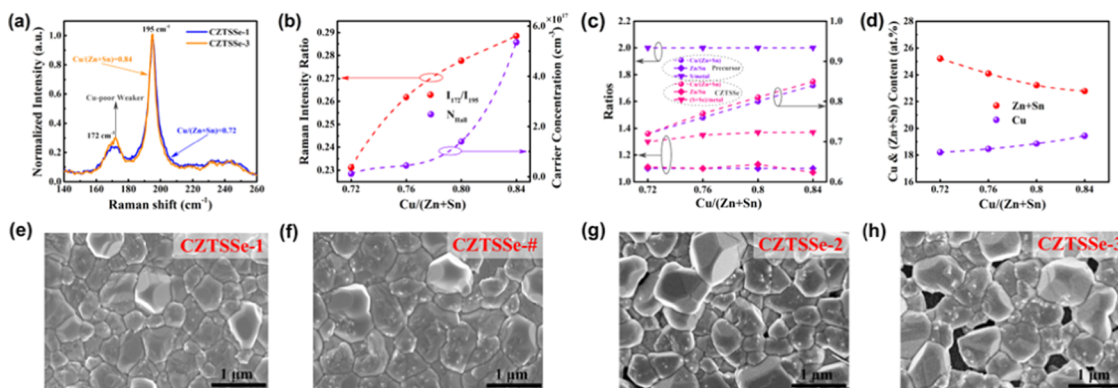


Figure 2. (a) Raman spectra of CZTSSe-1 and CZTSSe-3, and the intensity of which has been normalized. (b) Variations of Raman scattering intensity ratio I_{172}/I_{195} and carrier concentration of CZTSSe films. (c) Comparison between the composition ratios of Cu/(Zn + Sn), Zn/Sn and (S + Se)/metal in the precursor solution and CZTSSe films. (d) Variations of Cu and (Zn + Sn) contents in the CZTSSe films. Top-view SEM images of CZTSSe films involving different Cu/(Zn + Sn) of (e) 0.72, (f) 0.76, (g) 0.80, and (h) 0.84, respectively.

ray diffractometer with Cu $K\alpha$ radiation ($\lambda = 1.5406 \text{ \AA}$). Raman spectra with 473 nm excitation were conducted by a Horiba Jobin Yvon HR800 confocal Raman system. The cross-sectional and surface morphologies were investigated using a HITACHI S-4800 field-emission scanning electron microscope (FE-SEM) with an energy-dispersive X-ray spectroscopy (EDS) system (EDAX Genesis 2000). EDS was executed by a Si-drift detector attached to SUTW-Sapphire under an accelerating voltage of 17 keV. The electrical properties were determined via Hall-effect measurements with van der Pauw configuration in an electrical transport property measurement system (Lake Shore 7600 Hall measurement system). The current density–voltage (J – V) curve was obtained by a Keithley 2400 source meter under simulated AM 1.5G solar illumination, which has been calibrated to 100 mW cm^{-2} with a Newport official certified crystalline Si reference cell. A Zolix SCS100 QE system equipped with a 150 W xenon light source, an integrating sphere, and a lock-in amplifier was used to obtain the external quantum efficiency (EQE) curves. The C – V measurement was executed with a 20 mV and 100 kHz alternating current (AC) excitation source with a DC bias from -1 to 0 V under dark conditions.

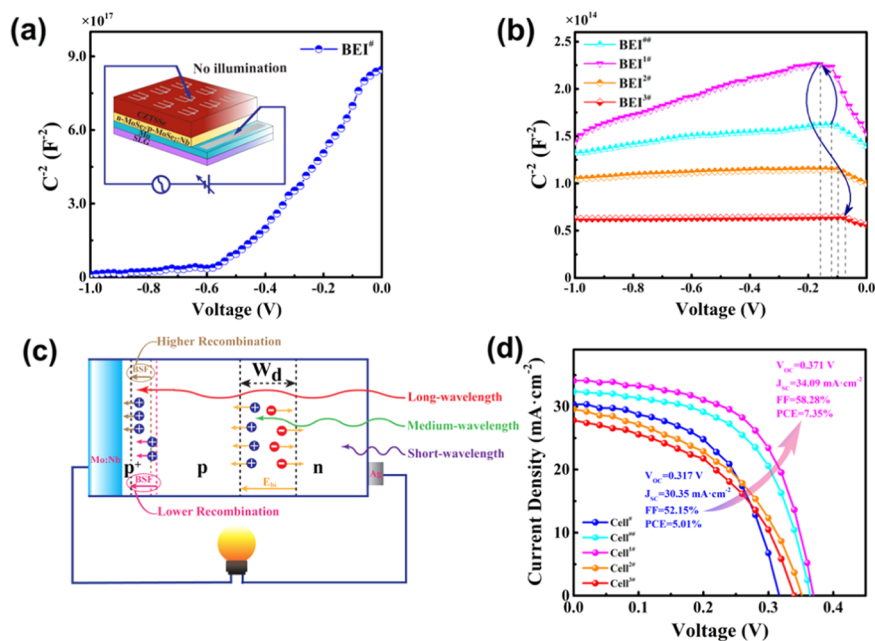
3. RESULTS AND DISCUSSION

To investigate the structural properties of CZTSSe films with various Cu/(Zn + Sn), XRD and Raman spectra measurements were implemented. Figure 1a depicts the XRD patterns of CZTSSe films grown on the SLG/Mo substrate. To identify these diffraction peaks, the standard PDF line patterns of CZTS (PDF#26–0575) and CZTSe (PDF#52–0868) are displayed in Figure 1a, too. This enables us to demonstrate the kesterite CZTSSe formation directly. It is noted that the

other possible impurities (e.g., ZnSe, Cu_2Se , etc.) were not detected. Also, the amplifying view of (204) diffraction peaks and their corresponding 2θ variation are displayed in Figure 1b,c, respectively. Evidently, the peak shifts slightly toward the lower angle with increasing Cu/(Zn + Sn), manifesting the increased lattice parameters as the larger Cu^+ ions (0.77 \AA) substitute the smaller Zn^{2+} (0.74 \AA) ions.³³ Then, it can be deduced from this variation that more Cu_{Zn} defects involved in the sample with the higher Cu/(Zn + Sn) because of the low formation energy of Cu_{Zn} .³⁴ Besides, it must also be mentioned that the diffraction peak shift is probably associated with S/Se variation in CZTSSe films. From Table S3 (Supporting Information), we observe that S/Se increases with increasing Cu/(Zn + Sn), and it should lead to a higher 2θ , but actually, we have not seen such variations in Figure 1b,c. Therefore, we consider that the low angle shift of the (204) peak is attributed to the increased Cu content, rather than the S amount change. As a matter of fact, the result that 2θ of the (204) plane becomes smaller when S/Se increases exactly supports the aforementioned viewpoint. It is well known that the characteristic XRD peaks of $\text{Cu}_2\text{Sn}(\text{S},\text{Se})_3$ and $\text{Zn}(\text{S},\text{Se})$ impurities are similar to that of CZTSSe, and therefore, it is hard to distinguish these second phases via an XRD method. To further identify the purity of CZTSSe films, we performed a Raman spectrum measurement using a 473 nm excitation source, as exhibited in Figure 1d. Raman vibration modes centered at 172, 195, 233, and 245 cm^{-1} are observed and regarded as the kesterite CZTSSe vibration, while the vibration

Table 1. Hall-Effect Measurement Results of CZTSSe Films with Various Cu/(Zn + Sn), Comprising the Resistivity (ρ), Carrier Concentration (N_{Hall}), Mobility (μ), and Conduction Type

sample	Cu/(Zn + Sn)	ρ [Ω cm]	N_{Hall} [cm^{-3}]	μ [$\text{cm}^2 \text{V}^{-1} \text{s}^{-1}$]	type
CZTSSe-1	0.72	1.26×10^2	1.16×10^{16}	4.09×10^0	p
CZTSSe-#	0.76	7.51×10^1	4.45×10^{16}	1.78×10^0	p
CZTSSe-2	0.80	3.59×10^1	1.40×10^{17}	1.19×10^0	p
CZTSSe-3	0.84	1.80×10^1	5.35×10^{17}	6.43×10^{-1}	p

**Figure 3.** (a, b) C^{-2} - V curves of buffer layer-free and window layer-free devices (named BEI^{1#}, BEI^{2#}, BEI^{3#}, BEI[#], and BEI[#]) involving different BEI structures (Table 2), respectively. The measurement schematic diagrams are displayed in the (a) inset. (c) Schematics of the influence of the BSF width distribution in the absorber on the photoinduced carrier transportation. (d) Light J - V curves of CZTSSe solar cells with a tunable BSF at AM 1.5G illumination, where the area of the cell is 0.19 cm^2 .

mode located at 327 cm^{-1} is indexed as the S ion mode in CZTSSe.^{35,36} Apart from that, no other impurity modes are revealed, coinciding with the XRD results. Remarkably, the scattering intensity of the 327 cm^{-1} mode is greatly weaker than that of the 195 cm^{-1} mode (Se ion vibration), indicating a low sulfur content,³⁷ which is consistent with the XRD results revealing a negligible difference in the diffraction peak position between the samples and the CZTSe phase (PDF#52-0868) (Figure 1a). Consequently, highly selenized CZTSSe films were prepared.

To further identify the weaker Cu-poor state of the CZTSSe film with higher Cu/(Zn + Sn), we selected Raman spectra of CZTSSe-1 and CZTSSe-3, as shown in Figure 2a, the scattering intensity of which has been normalized. It is seen that the Raman intensity ratio (I_{172}/I_{195}) of the vibration modes at 172 cm^{-1} with respect to that at 195 cm^{-1} increases with increasing Cu/(Zn + Sn), as clearly plotted in Figure 2b. Dimitrievska et al.³⁸ reported that the $[V_{\text{Cu}} + Z_{\text{Cu}}]$ defect cluster concentration decreased with increasing I_{172}/I_{195} , while the Raman intensity of 172 cm^{-1} increased with increasing Cu content.³⁹⁻⁴¹ Therefore, combining these two perspectives, it is reasonable to conclude that the CZTSSe film with higher Cu/(Zn + Sn) possesses fewer V_{Cu} and more Cu_{Zn} acceptor defects,³⁴ further in support of the XRD section deduction. These point defects in the CZTSSe film are commonly caused by the nonstoichiometry in the chemical composition. Furthermore, the formation energy of Cu_{Zn} (0.01 eV) is

much lower than that of V_{Cu} (0.57 eV) because a much smaller chemical potential disparity is observed between Cu and Zn compared to that of Cu and a vacancy.³⁴ Thus, Cu_{Zn} defects are dominant acceptors and lead to the p-type behavior of the CZTSSe film. As a result, we propose that the carrier concentration of CZTSSe should be increased as Cu/(Zn + Sn) increases (i.e., higher Cu_{Zn} acceptor defect concentration). Experimentally, we indeed observe a monotonic increase in the carrier concentration (N_{Hall}) of the p-CZTSSe film via Hall-effect measurement, when Cu/(Zn + Sn) varies from 0.72 to 0.84, as shown in Table 1 and Figure 2b.

To investigate the effect of Cu/(Zn + Sn) on the CZTSSe film morphology, SEM measurement was presented, as shown in Figure 2e-h. It is found that the morphology of CZTSSe films has a close dependence on Cu/(Zn + Sn). CZTSSe-1 and CZTSSe-# with relatively lower Cu/(Zn + Sn) have a compact surface without pinholes. This feature is favorable to the decrease of photoinduced carrier recombination at the grain boundaries and then facilitates carrier transportation.⁴² However, a further increase in Cu/(Zn + Sn) gives rise to polyporous morphology with a greater density of pinholes. Especially, a less uniform grain size distribution occurs on the surface, leading to aggravated carrier recombination. It was reported that excess Cu was implemented to grow a CIGS film with large grains since CuSe with a low melting point (flux role) formed under Cu-rich conditions.^{43,44} In contrast, a negative effect of increased Cu was found for CZTSSe films in

Table 2. Detailed Photovoltaic Parameters of CZTSSe Solar Cells

cell	BEI structure	V_{OC} [V]	J_{SC} [mA cm^{-2}]	FF [%]	PCE [%]
Cell [#]	Mo/n-MoSe ₂ /CZTSSe-#/CZTSSe-#	0.317	30.35	52.15	5.01
Cell ^{##}	Mo:Nb/p-MoSe ₂ :Nb/CZTSSe-#/CZTSSe-#	0.365	32.37	56.11	6.62
Cell ^{1#}	Mo:Nb/p-MoSe ₂ :Nb/CZTSSe-1/CZTSSe-#	0.371	34.09	58.28	7.35
Cell ^{2#}	Mo:Nb/p-MoSe ₂ :Nb/CZTSSe-2/CZTSSe-#	0.352	29.61	45.99	4.79
Cell ^{3#}	Mo:Nb/p-MoSe ₂ :Nb/CZTSSe-3/CZTSSe-#	0.343	27.13	43.53	4.05

Table 3. Electric Parameters for CZTSSe Solar Cells

cell	R_S [$\Omega \text{ cm}^2$]	R_{Sh} [$\Omega \text{ cm}^2$]	G_{Sh} [mS cm^{-2}]	A	J_0 [mA cm^{-2}]	R_C/R_{Sh}	R_S/A
Cell [#]	0.32	143.27	6.98	2.63	2.50×10^{-1}	0.0022	0.122
Cell ^{##}	0.30	653.59	1.53	2.48	9.22×10^{-2}	0.0005	0.121
Cell ^{1#}	0.38	413.22	2.42	2.14	3.71×10^{-2}	0.0009	0.178
Cell ^{2#}	0.57	111.33	8.98	3.00	2.80×10^{-1}	0.0051	0.190
Cell ^{3#}	0.97	173.61	5.76	3.04	3.02×10^{-1}	0.0056	0.319

this work and also other reports,^{45,46} contradicting with Cu-assisted grain growth in the CIGS case, which can be elucidated as below. Tables S2,S3 (Supporting Information) display the chemical compositions of CZTS precursor solution and CZTSSe films grown on the SLG substrate measured by EDS. To minimize the possible measurement deviation, six different regions were selected to get accurate composition information for every sample. Interestingly, we observed from Figure 2c that the variation of Cu/(Zn + Sn) in the CZTSSe film exhibits the same tendency as that in precursor solution and the former is slightly higher than the latter due to Zn and/or Sn losses. Meanwhile, increasing Cu/(Zn + Sn) leads to decreased Zn and/or Sn in CZTSSe films. Given that Sn or Zn in precursor solution could exist as oxides, hydroxides, or other complexes that can be melted during selenization, as a result, they play a positive flux role to facilitate CZTSSe grain growth.⁴⁵ Therefore, the loss of Zn and/or Sn resulted in the voids distributed on the surface of CZTSSe-2 and CZTSSe-3. Also, Figure 2d shows a plot of the Cu and (Zn + Sn) content variation with increasing Cu/(Zn + Sn). Higher Cu content is obtained, whereas the (Zn + Sn) content becomes lower as Cu/(Zn + Sn) increases. Then, this result should be of a direct indication to the more Cu_{Zn} acceptors involved in the CZTSSe films, while Cu/(Zn + Sn) varies from 0.72 to 0.84, as revealed in the XRD and Raman spectra discussions. In addition, the (S + Se) atom % is somewhat higher compared to the stoichiometric value of 50%, which is reasonably attributed to the experimentally applied excess selenium. The excess selenium employed in the CZTSSe film growth is commonly accepted and demonstrated to depress the loss of Sn during the selenization process.⁴⁷

As discussed above, we have obtained CZTSSe films having various carrier concentrations. As is known to all, the depletion layer width distribution of p–n junction becomes wider with decreasing the corresponding carrier concentration. Furthermore, it has been proven that carrier recombination at the BEI reduced effectively after BSF incorporation.^{25,26} Therefore, it is critical to modulate the BSF width distribution in the absorber for efficient carrier transportation, i.e., decrease in electricity loss (EL) and increase in solar cell performance, respectively. This distribution modulation was realized via tuning the carrier concentration in the absorber, which can be validated by $C-V$ characterization. Figure 3a,b shows the $C^{-2}-V$ curves of buffer layer-free and window layer-free devices (named BEI[#], BEI^{##}, BEI^{1#}, BEI^{2#}, and BEI^{3#}) involving different BEI structures

(Table 2), respectively. BEI[#] has a Mo electrode and a built-in electric field from MoSe₂ to the absorber, while the other devices contain a Mo:Nb electrode and an inverse field orientation from the absorber to MoSe₂:Nb. All devices possess the same top electrode Ag. The measurement schematic diagram is displayed in the inset of Figure 3a. For the case of BEI[#], the C^{-2} decreases, i.e., C increases as the negative bias voltage increases. This variation is indicative of the partial carriers' deposit and the narrower depletion layer, which indirectly reflect the built-in potential orientation toward the absorber at the BEI due to the presence of an n-MoSe₂ interfacial layer. This undesirable potential orientation exerts a bad effect on the carrier separation at the BEI as the solar cell works. In contrast, for the cases of BEI^{##}–BEI^{3#} (Figure 3b), the C^{-2} increases first and then decreases, i.e., C decreases first and then increases with increasing negative bias voltage. This phenomenon indicates that partial carriers were first extracted and then deposited again to the BEI under a higher voltage owing to the presence of the BSF.⁴⁸ Differing from the BEI[#] case, beneficially, the built-in field or the BSF orientation is from the absorber to the back electrode, which capacitates more effective transportation of holes and electrons toward the back and front electrodes, respectively. Moreover, the threshold voltage initially increases from BEI^{##} to BEI^{1#}, while it decreases from BEI^{1#} to BEI^{3#}. Considering that the barrier capacitance of the p–n junction under negative bias voltage is equivalent to the capacitance in a parallel-plate capacitor, and accordingly, the barrier region width corresponds to the distance between parallel plates. Higher negative bias voltage leads to a wider barrier region, consequently reducing the capacitance in the p–n junction.⁴⁸ Then, it is implied that a higher threshold voltage means a wider BSF distribution as in Figure 3b, i.e., the BSF width distribution in the absorber becomes wider from BEI^{##} to BEI^{1#}, whereas it gradually turns narrower from BEI^{1#} to BEI^{3#}.

To study the influence of the BSF width distribution in the absorber on the solar cell performance, we fabricated a series of CZTSSe solar cells named Cell[#], Cell^{##}, Cell^{1#}, Cell^{2#}, and Cell^{3#} with different BEI structures, as listed in Table 2. As shown in Figure 3c, light absorption of the photons assigned to long wavelengths at the BEI is an important component for the photogenerated current. Hence, the wider BSF distribution in the absorber should lead to a lower EL considering the critical role of the BSF in facilitating carrier transportation. Figure 3d depicts the photocurrent density–voltage ($J-V$) plots of

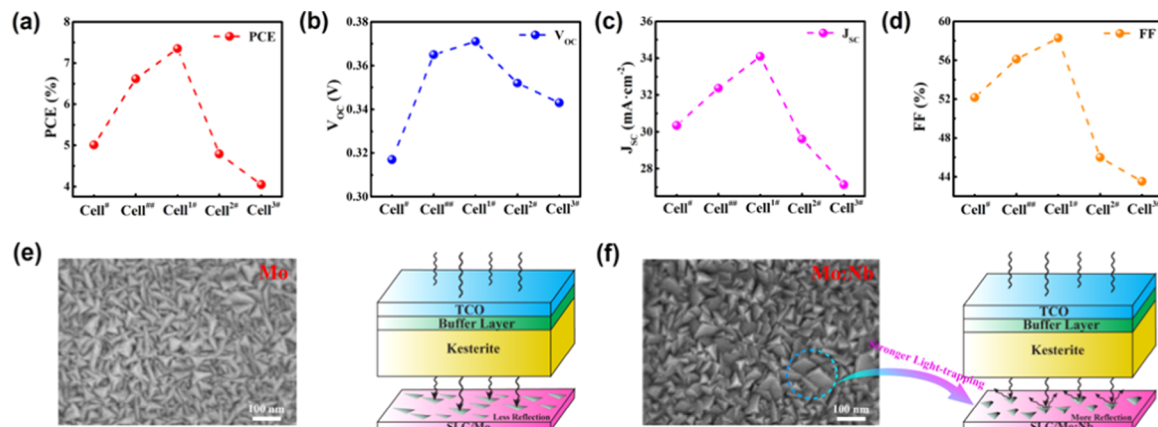


Figure 4. Variations of (a) PCE, (b) V_{OC} , (c) J_{SC} , and (d) fill factor (FF) for Cell[#], Cell^{##}, Cell^{1#}, Cell^{2#}, and Cell^{3#}, respectively. (e, f) SEM morphologies of Mo and Mo:Nb films grown on the SLG substrate, respectively. Also, a schematic diagram of the light utilization difference between two electrodes is included; the Mo:Nb electrode with pyramidal morphology exhibits a stronger light-trapping effect due to higher back reflectivity.

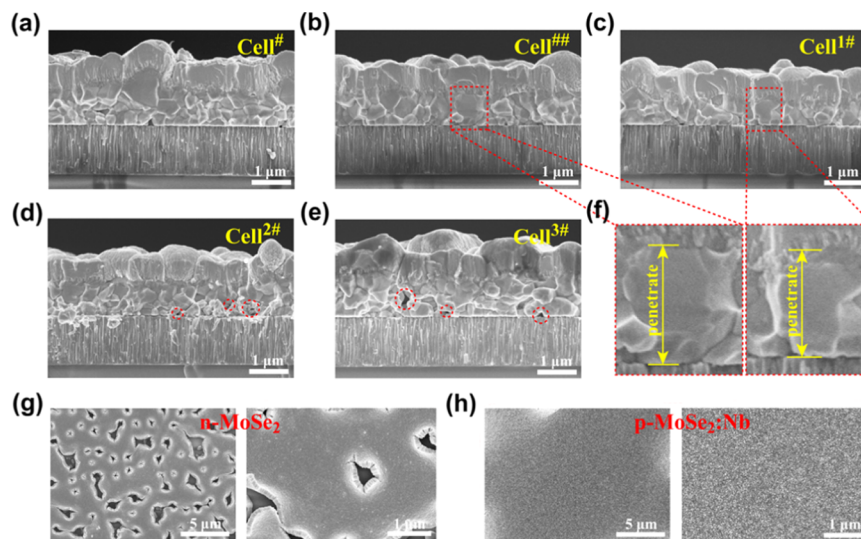


Figure 5. Cross-sectional SEM images of (a) Cell[#], (b) Cell^{##}, (c) Cell^{1#}, (d) Cell^{2#}, and (e) Cell^{3#}, respectively. (f) Enlarged view of the absorber region for Cell^{##} and Cell^{1#}. Some large grains vertically penetrate through the whole absorber region, which suppresses the recombination at grain boundaries and facilitates carrier transportation. (g, h) SEM morphology of MoSe₂ and MoSe₂:Nb, respectively. The compact and void-free morphology in MoSe₂:Nb mitigates the shunting problem to some extent.

CZTSSe solar cells with various BEI structures, respectively. Tables 2 and 3 list the detailed photovoltaic and electric parameters. Also, the variations of photovoltaic parameters are plotted in Figure 4a–d. From Figure 4a, it is noteworthy that the PCE has experienced an appreciable increase from 5.01% (Cell[#]) to 6.62% (Cell^{##}) after introducing a BSF, which mainly benefits from higher V_{OC} and J_{SC} values due to the increased R_{Sh} and the decreased reverse saturation current density (J_0). Thus, it is essential to gain insight into the role of the BSF in improving the device performance, as analyzed below.

BSF-induced local passivation to the back electrode brings about a reduction in electric leakage, and as a consequence, R_{Sh} increases.^{49–51} Moreover, the decreased recombination velocity at the BEI due to the BSF effect results in a decrease in J_0 from 2.50×10^{-1} (Cell[#]) to 9.22×10^{-2} (Cell^{##}) mA cm⁻²,^{25,49} facilitating J_{SC} improvement. Then, given that V_{OC} is inversely proportional to J_0

$$G_{Sh}V_{OC} = J_{SC} - J_0(e^{qV_{OC}/kT} - 1) \quad (1)$$

where G_{Sh} , q , A , k , and T are the shunt conductance, electron charge, diode ideality factor, Boltzmann constant, and temperature, respectively.⁵² A higher V_{OC} value is obtained with the incorporation of the BSF, further considering the increased R_{Sh} , as shown in eq 2.⁵³

$$V_{OC} = \frac{AkT}{q} \ln \left(\frac{J_{SC} - V_{OC}/R_{Sh}}{J_0} + 1 \right) \quad (2)$$

In a word, the decrease in J_0 plays the main role in the increase of J_{SC} , V_{OC} , and PCE accordingly due to the BSF application. As far as the positive effect of the BSF is concerned, Omrani et al.²⁸ reported that the back surface recombination current of CZTSSe solar cells can be decreased to be one order of magnitude using SnS as the BSF layer via SCAPS simulation, making enhancements in V_{OC} and J_{SC} , too. Khattak et al.²⁹ also achieved a similar simulation result

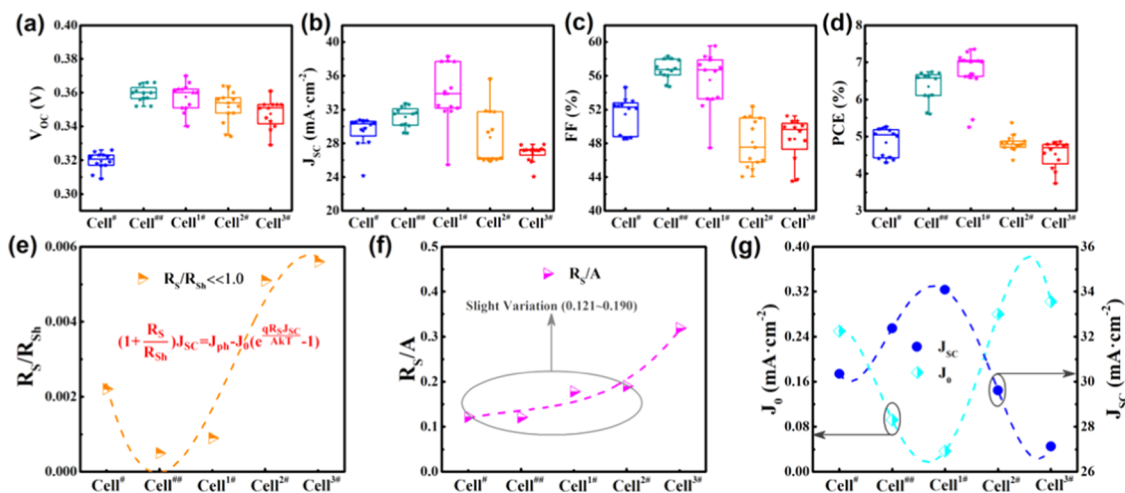


Figure 6. Statistical parameters including (a) V_{OC} , (b) J_{SC} , (c) FF, and (d) PCE of CZTSSe solar cells without and with the BSF, respectively. BSF-applied cells (Cell^{##}–Cell^{3#}) realized an appreciable V_{OC} increment, and the J_{SC} and FF also have been improved effectively via BSF modulation. Variations of (e) R_S/R_{Sh} , (f) R_S/A , and (g) J_0 & J_{SC} for CZTSSe solar cells with a tunable BSF, respectively.

utilizing CZTSe as the BSF layer in CTZS solar cells. Therefore, our experimental results convincingly validate the simulation prediction. Another interesting finding from Figure 4a and Table 2 is that a peak PCE of 7.35% (Cell^{1#}) is obtained after applying the bottom absorber with a lower carrier concentration to the BEI as compared to that of Cell^{##}. The champion cell has a high V_{OC} of 0.371 V, high J_{SC} of 34.09 mA cm⁻², and excellent fill factor (FF) of 58.28%. Remarkably, J_{SC} has achieved a further improvement from 32.37 (Cell^{##}) to 34.09 mA cm⁻² (Cell^{1#}), which is mainly responsible for a further increase in PCE. It is ascribed to the continuously lower J_0 induced by the wider BSF distribution in the absorber. Noting that the BSF-applied Cell^{##} and Cell^{1#} have obtained a substantial improvement in J_{SC} as compared to that of the BSF-free Cell[#]. Aside from the BSF effect, the other nonignorable factor is the light-trapping effect difference between Mo and Mo:Nb back electrodes. As shown in Figure 4e,f, Mo has smooth surface morphology, while that for Mo:Nb possesses pyramidal morphology. This modified morphology leads to higher back electrode reflectivity, and thus, a stronger light-trapping effect is exhibited, i.e., smaller optical losses and higher J_{SC} values.^{54,55}

On the contrary, increasing the carrier concentration of the bottom absorber in comparison with that of Cell^{##} causes a dramatic deterioration in device performances (Cell^{2#} and Cell^{3#}), especially J_{SC} , FF, and PCE (Figure 4a–d). This result can be elucidated from two aspects: (i) As a result of the narrower BSF distribution in the absorber, the corresponding J_0 values of Cell^{2#} and Cell^{3#} increase continuously compared to Cell^{1#}. The recombination variation is also indicated from the variation tendency of A , which decreases initially from 2.63 to the superior 2.14 and then increases up to the inferior value 3.04, as shown in Table 3; (ii) It is explained from the perspective of interface crystalline quality. As illustrated in Figure 5d,e, the grains of the bottom absorber for Cell^{2#} and Cell^{3#} are small with some pinholes, which verify the observation again from Figure 2g,h. It is commonly known that recombination of photoinduced carriers usually occurs at grain boundaries, decreasing the current density. Hence, this polyporous cross-sectional morphology results in more serious recombination, which is partially responsible for their evidently larger J_0 . Also, some pinholes comprised in the BEI region

lower down R_{Sh} to relatively smaller values of 111.33 and 173.61 Ω cm² for Cell^{2#} and Cell^{3#}, respectively (Table 3).^{15,53} Therefore, it is concluded that the distinctly lower R_{Sh} and larger J_0 lead to drastic degradation of photovoltaic performance for Cell^{2#} and Cell^{3#}. By comparison, differing from the defective cross-sectional SEM morphologies in Cell^{2#} and Cell^{3#}, the favorable absorbers comprising larger grains without pinholes are observed for Cell[#], Cell^{##}, and Cell^{1#} (Figure 5a–c), being beneficial for device performance since the recombination at grain boundaries decreases.⁴² Particularly, some large grains contained in Cell^{##} and Cell^{1#} vertically penetrate through the whole absorber region, as presented in Figure 5f. This characteristic morphology can mitigate the recombination of photoinduced carriers at grain boundaries and facilitate carrier transportation to a larger extent.^{5,56,57} The outstanding absorber crystalline quality in Cell^{##} and Cell^{1#} is not only attributed to the component superior CZTSSe-1 and CZTSSe-# as revealed in Figure 2e–h discussion but also to the compact surface without voids in interfacial layer p-MoSe₂:Nb as compared to that of n-MoSe₂, as shown in Figure 5g,h. Noting that although the same component absorber was employed for Cell[#] and Cell^{##}, two devices differ remarkably in the absorber quality via the observation of Figure 5a,b. It is reported that the influence of the environment on sodium distribution is negligible⁵⁸ and should be consistent on both Cell[#] and Cell^{##}, and therefore, it is believed that the difference in absorber quality should be associated with BEI modification. This is because the pinholes distributed in the n-MoSe₂ surface can serve as a spatial barrier,¹⁵ penalizing sodium diffusion from the SLG substrate into the absorber and suppressing the grain growth. Furthermore, the locally blocked sodium diffusion may cause a heterogeneous sodium distribution, which probably account for the nonuniform absorber grain size in Figure 5a, as shown in Figure S2 (Supporting Information). In addition, as for the undesirable role of pinholes or voids in aggravating the shunting problem,^{15,59} the void-free surface morphology of p-MoSe₂:Nb is partially responsible for the increased R_{Sh} from Cell[#] to Cell^{##}.

The statistical parameters including (a) V_{OC} , (b) J_{SC} , (c) FF, and (d) PCE are illustrated in Figure 6a–d. All of the BSF-applied cells have realized an expected V_{OC} enhancement. The J_{SC} , FF, and PCE accordingly can be improved effectively by

optimizing the BSF width distribution, especially in Cell^{##} and Cell^{1#}. To well understand the J_{SC} variation after introducing the BSF, the relations between series resistance (R_S), R_{Sh} , A , J_0 , and J_{SC} are investigated, given that J_{SC} can be expressed as

$$\left(1 + \frac{R_S}{R_{Sh}}\right) J_{SC} = J_{ph} - J_0(e^{qR_S J_{SC}/AkT} - 1) \quad (3)$$

where J_{ph} denotes photogenerated current density.⁵² It is speculated that the increased or decreased J_{SC} originates from the lower or higher values of R_S/R_{Sh} , J_0 , and R_S/A . Figure 6e–g shows a plot of the variations of R_S/R_{Sh} , R_S/A , J_0 , and J_{SC} for five cells, respectively. Obviously, R_S/R_{Sh} exerts a negligible impact on J_{SC} due to their small values far less than 1.0. Regarding the R_S/A , its value changes slightly (0.121–0.190) except for the Cell^{3#} case. Consequently, it can be concluded that J_0 is the dominant factor for J_{SC} variation, at least for cells Cell[#], Cell^{##}, Cell^{1#}, and Cell^{2#}. Interestingly, the inverse correlation between J_{SC} and J_0 observed from Figure 6g also validates the aforementioned analysis. For the worst device Cell^{3#}, the evidently higher R_S and lower R_{Sh} play the dominating role in governing J_{SC} variation with an eye to its apparently higher values of R_S/R_{Sh} and R_S/A (Figure 6e,f) compared to that of the other four cells, in addition to the other critical factor J_0 . Then, the corresponding J_{SC} decreases distinctly. Besides, extraordinarily low R_S values below 0.6 Ω cm² are exhibited for Cell[#], Cell^{##}, Cell^{1#}, and Cell^{2#}. Indeed, from the perspective of R_S , our work owns an equivalent level to that of CZTSSe solar cells with superior performance,^{5,60} as displayed in Table 4. As is known to all, overselenization

Table 4. Comparison between This Work and References (ref) in R_S

	back electrode configuration	R_S [Ω cm ²]
this work	Mo-H/Mo-L/Mo-H or Mo:Nb-H/Mo:Nb-L/Mo:Nb-H	0.30–0.97
ref 5	unknown	0.72
ref 60	unknown	0.96

usually takes place in the process of selenization, resulting in a thicker interfacial layer MoSe₂, and then R_S increases dramatically.⁶¹ Moreover, it has been demonstrated that the Mo film sputtered at a low working pressure (Mo-L) can be selenized more easily compared to the one sputtered at a high working pressure (Mo-H).⁶² Therefore, the back electrode configuration was fabricated with an improved stack order of Mo-H/Mo-L/Mo-H or Mo:Nb-H/Mo:Nb-L/Mo:Nb-H in this work instead of a traditional bilayer structure (Table 4). The main reason is that an additional top Mo-H or Mo:Nb-H can play the role of buffer in preventing overselenization to some degree, thereby achieving a favorable R_S value.

EQE is an effective characterization technique to analyze the performance of solar cells, and the impact of the BSF on the recombination at the BEI can also be investigated via this characterization. Figure 7a displays the EQE spectra of Cell[#], Cell^{##}, Cell^{1#}, Cell^{2#}, and Cell^{3#}, respectively. Cell^{##} and Cell^{1#} own a superior EQE, which is in good agreement with their outstanding photovoltaic properties. Obviously, the EQE variation below \sim 550 nm can be negligible for all devices, whereas it improves evidently in the long-wavelength region as the incorporation of a wider BSF distribution. This EQE offset suggests that the BSF-applied device can utilize the long-

wavelength incident light more effectively due to the depression of recombination and improvement of photo-induced hole collection in the BEI region, as illustrated in Figure 3c. Also, it reveals a smaller EL derived from the incomplete collection of photoinduced carriers in the absorber, as discussed in J – V results. The J_{SC} accuracy can be evaluated via integrating the EQE spectrum using the equation below

$$J_{SC} = q \int_0^\infty F_{1.5}(\lambda) EQE(\lambda) d\lambda \quad (4)$$

where $F_{1.5}(\lambda)$ represents the density of incident photons at AM 1.5G solar illumination. As shown in Figure 7b, the integrated current densities of Cell[#], Cell^{##}, Cell^{1#}, Cell^{2#}, and Cell^{3#} from the EQE spectrum were calculated to be 30.27, 31.59, 33.57, 29.79, and 26.78 mA cm⁻², respectively. These values are in accordance with the measured device characteristics (Table 2), and the small mismatch confirms the accuracy of J – V measurements. Besides, the E_g of the absorber is extracted from the x -axis intercept in the Tauc plot [$hv \times \ln(1 - EQE)$]² versus hv ,^{63,64} where hv denotes the photon energy, as presented in Figure 7c. It can be observed that E_g values have no obvious change since the same top absorber (CZTSSe-#) is applied for five cells. They are in the range of 1.088–1.096 eV, corresponding to the reported E_g of CZTSSe solar cells.^{6,60}

As far as the collection ability of photoinduced carriers is concerned, under no circumstances can we neglect a crucial factor of the depletion layer width (W_d). Considering that photons assigned to long wavelengths are mainly absorbed in the bottom absorber (Figure 3c) owing to the fact that the absorption coefficient becomes smaller with increasing light wavelength. As a result, the serious EL occurs in the bottom absorber region beyond the scope of W_d . To obtain W_d values, we performed C – V measurement, as shown in Figure 7d,e. The W_d values of Cell[#], Cell^{##}, Cell^{1#}, Cell^{2#}, and Cell^{3#} were calculated to be 120, 118, 133, 122, and 131 nm, respectively, as plotted in Figure 7f. The calculated method can be found elsewhere.^{21,65} The slight variation in W_d is attributed to the otherwise identical experimental conditions of the top absorber and CdS/i-ZnO/ITO for all devices. Noting that Cell[#] and Cell^{##} adopt a single absorber structure, while the other cells employ the double absorber structure. Additionally, more favorable cross-sectional SEM morphologies comprising larger grains without pinholes are observed for both Cell^{##} and Cell^{1#}. Thus, for the Cell^{##} and Cell^{1#}, the superior EQE (Figure 7a) is attributed to the better absorber quality (from \sim 600 to \sim 900 nm) and wider BSF (from \sim 900 to \sim 1100 nm) as compared to the referenced BSF-free Cell[#]. To sum up, the appreciable increase in the long-wavelength EQE spectrum (i.e., a decrease in electricity loss) validates the feasibility of field-effect passivation modulation applied in this work. Consequently, combining the aim of this study, i.e., BSF width distribution in the absorber, C – V and EQE results enable us to determine that the slightly changed W_d values (average value, 124.8 nm) can be ignored when analyzing J_{SC} variation, and the BSF effect is at the heart of the problem, supporting the validity of J – V analysis.

4. CONCLUSIONS

BEI recombination is an important element impeding further progress of kesterite-type CZTSSe solar cells. Using field-effect passivation with the BSF can address this issue to some degree. From XRD and Raman results, it has been revealed that more Cu_{Zn} defects involved in CZTSSe films with higher Cu/(Zn +

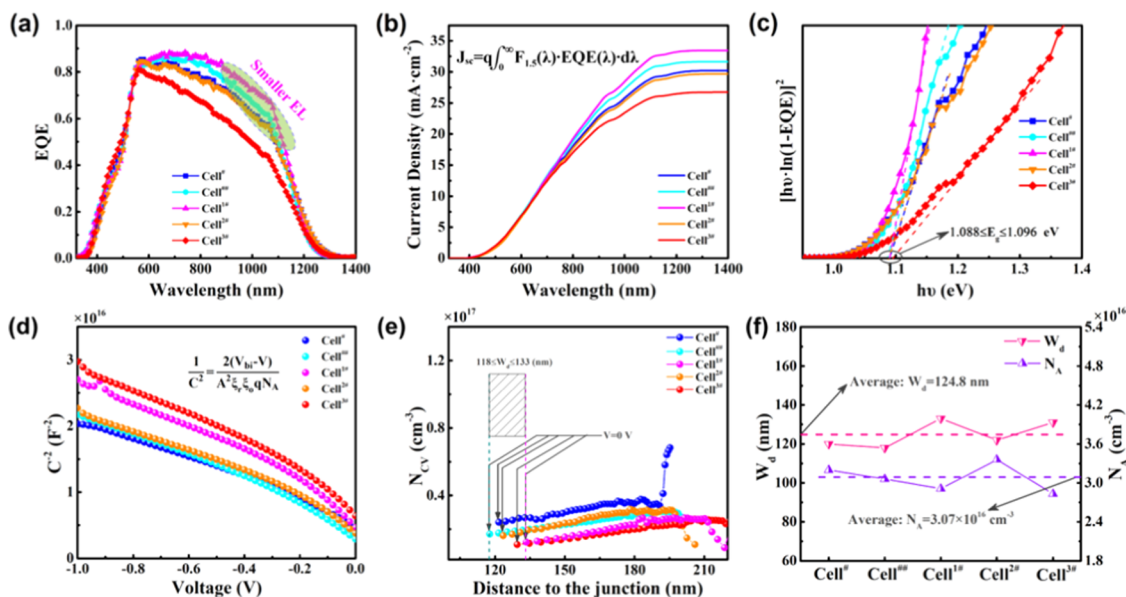


Figure 7. (a) EQE spectra and (b) integrated current density of CZTSSe solar cells without and with the BSF. (c) E_g of absorbers obtained via extrapolating the Tauc plot $[hv \times \ln(1 - EQE)]^2$ versus $h\nu$ to the x -axis. Plots of (d) C^{-2} versus bias voltage, (e) $C-V$ profiling, and (f) variations of W_d and N_A for CZTSSe solar cells, respectively.

Sn). The tunable BSF distributed in the absorber is realized by modulating the carrier concentration of the absorber, which is validated by $C-V$ characterization. Over 7% efficiency of BSF-applied solar cells was obtained via optimizing the BSF width distribution, which mainly originates from higher V_{OC} and J_{SC} values due to an increase in R_{Sh} and a decrease in J_0 . The BSF-induced local passivation to the back electrode is responsible for the increased R_{Sh} . Also, the compact and void-free morphology in $MoSe_2:Nb$ mitigates the shunting problem to some extent, and then, higher R_{Sh} is obtained. By analyzing the variation tendency of R_S/R_{Sh} , R_S/A , and J_0 , it is determined that J_0 is the dominant factor for J_{SC} variation. The decrease of J_0 is attributed to the depressed BEI recombination as BSF incorporation and the favorable cross-sectional absorber morphology. Remarkably, a small R_S value below $0.6 \Omega \text{ cm}^2$ is exhibited owing to the improved trilayer back electrode configuration. In addition, the decreased BEI recombination after optimizing the BSF effect is also demonstrated by the evidently smaller EL from the EQE spectrum, which validates the feasibility of field-effect passivation modulation for device performance improvement. Expectantly, this study will be reminiscent of the importance of BSF that has been applied commonly in Si-based and CIGS-based solar cells. Therefore, BSF applications for CZTSSe-based solar cells have been motivating more research studies in photovoltaic communities.

ASSOCIATED CONTENT

Supporting Information

The Supporting Information is available free of charge at <https://pubs.acs.org/doi/10.1021/acsami.0c10561>.

EDS spectrum of a $Mo:Nb$ film grown on the SLG substrate and statistical histograms of the absorber grain size distribution from the SEM images in Figure 5a,b; composition ratios in CZTS precursor solution; the compositions of $MoSe_2$ and $MoSe_2:Nb$ films measured via EDS and XPS and those of CZTSSe films prepared on the SLG substrate measured by EDS (PDF)

AUTHOR INFORMATION

Corresponding Authors

Bin Yao – State Key Laboratory of Superhard Materials and Key Laboratory of Physics and Technology for Advanced Batteries (Ministry of Education), College of Physics, Jilin University, Changchun 130012, P. R. China; orcid.org/0000-0003-0748-3220; Email: binyao@jlu.edu.cn

Yongfeng Li – State Key Laboratory of Superhard Materials and Key Laboratory of Physics and Technology for Advanced Batteries (Ministry of Education), College of Physics, Jilin University, Changchun 130012, P. R. China; orcid.org/0000-0002-9725-0692; Email: liyongfeng@jlu.edu.cn

Authors

Yanping Song – State Key Laboratory of Superhard Materials and Key Laboratory of Physics and Technology for Advanced Batteries (Ministry of Education), College of Physics, Jilin University, Changchun 130012, P. R. China

Huanhuan Sun – State Key Laboratory of Superhard Materials and Key Laboratory of Physics and Technology for Advanced Batteries (Ministry of Education), College of Physics, Jilin University, Changchun 130012, P. R. China

Zhanhui Ding – State Key Laboratory of Superhard Materials and Key Laboratory of Physics and Technology for Advanced Batteries (Ministry of Education), College of Physics, Jilin University, Changchun 130012, P. R. China

Wei Qin – State Key Laboratory of Superhard Materials and Key Laboratory of Physics and Technology for Advanced Batteries (Ministry of Education), College of Physics, Jilin University, Changchun 130012, P. R. China

Zhenzhong Zhang – State Key Laboratory of Luminescence and Applications, Changchun Institute of Optics, Fine Mechanics and Physics, Chinese Academy of Sciences, Changchun 130033, P. R. China

Ligong Zhang – State Key Laboratory of Luminescence and Applications, Changchun Institute of Optics, Fine Mechanics and Physics, Chinese Academy of Sciences, Changchun 130033, P. R. China

Haifeng Zhao – State Key Laboratory of Luminescence and Applications, Changchun Institute of Optics, Fine Mechanics and Physics, Chinese Academy of Sciences, Changchun 130033, P. R. China

Daocheng Pan – State Key Laboratory of Rare Earth Resource Utilization, Changchun Institute of Applied Chemistry, Chinese Academy of Sciences, Changchun 130022, P. R. China;

✉ orcid.org/0000-0002-8273-6331

Complete contact information is available at:
<https://pubs.acs.org/10.1021/acsami.0c10561>

Author Contributions

All authors have given approval to the final version of the paper.

Notes

The authors declare no competing financial interest.

ACKNOWLEDGMENTS

This work was supported by the National Natural Science Foundation of China under Grant Nos. 61774075, the Science and Technology Development Project of Jilin Province under Grant No. 20170101142JC, and the Natural Science Foundation of Jilin Province under Grant No. 20180101227JC. This work was also supported by the High Performance Computing Center of Jilin University, China.

REFERENCES

- (1) Katagiri, H.; Jimbo, K.; Maw, W. S.; Oishi, K.; Yamazaki, M.; Araki, H.; Takeuchi, A. Development of CZTS-Based Thin Film Solar Cells. *Thin Solid Films* **2009**, *517*, 2455–2460.
- (2) Repins, I.; Contreras, M. A.; Egaas, B.; DeHart, C.; Scharf, J.; Perkins, C. L.; To, B.; Noufi, R. 19.9%-Efficient ZnO/CdS/CuInGaSe₂ Solar Cell with 81.2% Fill Factor. *Prog. Photovoltaics: Res. Appl.* **2008**, *16*, 235–239.
- (3) Guo, Q.; Hillhouse, H. W.; Agrawal, R. Synthesis of Cu₂ZnSnS₄ Nanocrystal Ink and Its Use for Solar Cells. *J. Am. Chem. Soc.* **2009**, *131*, 11672–11673.
- (4) Jiang, F.; Ikeda, S.; Harada, T.; Matsumura, M. Pure Sulfide Cu₂ZnSnS₄ Thin Film Solar Cells Fabricated by Preheating an Electrodeposited Metallic Stack. *Adv. Energy Mater.* **2014**, *4*, No. 1301381.
- (5) Wang, W.; Winkler, M. T.; Gunawan, O.; Gokmen, T.; Todorov, T. K.; Zhu, Y.; Mitzi, D. B. Device Characteristics of CZTSSe Thin-Film Solar Cells with 12.6% Efficiency. *Adv. Energy Mater.* **2014**, *4*, No. 1301465.
- (6) Kim, J.; Hiroi, H.; Todorov, T. K.; Gunawan, O.; Kuwahara, M.; Gokmen, T.; Nair, D.; Hopstaken, M.; Shin, B.; Lee, Y. S.; Wang, W.; Sugimoto, H.; Mitzi, D. B. High Efficiency Cu₂ZnSn(S,Se)₄ Solar Cells by Applying a Double In₂S₃/CdS Emitter. *Adv. Mater.* **2014**, *26*, 7427–7431.
- (7) Son, D.-H.; Kim, S.-H.; Kim, S.-Y.; Kim, Y.-I.; Sim, J.-H.; Park, S.-N.; Jeon, D.-H.; Hwang, D.-K.; Sung, S.-J.; Kang, J.-K.; Yang, K.-J.; Kim, D.-H. Effect of Solid-H₂S Gas Reactions on CZTSSe Thin Film Growth and Photovoltaic Properties of a 12.62% Efficiency Device. *J. Mater. Chem. A* **2019**, *7*, 25279–25289.
- (8) Nakamura, M.; Yamaguchi, K.; Kimoto, Y.; Yasaki, Y.; Kato, T.; Sugimoto, H. Cd-Free Cu(In,Ga)(Se,S)₂ Thin-Film Solar Cell with Record Efficiency of 23.35%. *IEEE J. Photovoltaics* **2019**, *9*, 1863–1867.
- (9) Bourdais, S.; Choné, C.; Delatouche, B.; Jacob, A.; Larramona, G.; Moisan, C.; Lafond, A.; Donatini, F.; Rey, G.; Siebentritt, S.; Walsh, A.; Dennler, G. Is the Cu/Zn Disorder the Main Culprit for the Voltage Deficit in Kesterite Solar Cells? *Adv. Energy Mater.* **2016**, *6*, No. 1502276.
- (10) Gershon, T.; Lee, Y. S.; Antunez, P.; Mankad, R.; Singh, S.; Bishop, D.; Gunawan, O.; Hopstaken, M.; Haight, R. Photovoltaic

Materials and Devices Based on the Alloyed Kesterite Absorber (Ag_xCu_{1-x})₂ZnSnSe₄. *Adv. Energy Mater.* **2016**, *6*, No. 1502468.

(11) Gokmen, T.; Gunawan, O.; Todorov, T. K.; Mitzi, D. B. Band Tailing and Efficiency Limitation in Kesterite Solar Cells. *Appl. Phys. Lett.* **2013**, *103*, No. 103506.

(12) Kaur, K.; Kumar, N.; Kumar, M. Strategic Review of Interface Carrier Recombination in Earth Abundant Cu–Zn–Sn–S–Se Solar Cells: Current Challenges and Future Prospects. *J. Mater. Chem. A* **2017**, *5*, 3069–3090.

(13) Sun, K.; Yan, C.; Liu, F.; Huang, J.; Zhou, F.; Stride, J. A.; Green, M.; Hao, X. Over 9% Efficient Kesterite Cu₂ZnSnS₄ Solar Cell Fabricated by Using Zn_{1-x}Cd_xS Buffer Layer. *Adv. Energy Mater.* **2016**, *6*, No. 1600046.

(14) Lee, Y. S.; Gershon, T.; Todorov, T. K.; Wang, W.; Winkler, M. T.; Hopstaken, M.; Gunawan, O.; Kim, J. Atomic Layer Deposited Aluminum Oxide for Interface Passivation of Cu₂ZnSn(S,Se)₄ Thin-Film Solar Cells. *Adv. Energy Mater.* **2016**, *6*, No. 1600198.

(15) Liu, F.; Huang, J.; Sun, K.; Yan, C.; Shen, Y.; Park, J.; Pu, A.; Zhou, F.; Liu, X.; Stride, J. A.; Green, M. A.; Hao, X. Beyond 8% Ultrathin Kesterite Cu₂ZnSnS₄ Solar Cells by Interface Reaction Route Controlling and Self-Organized Nanopattern at the Back Contact. *NPG Asia Mater.* **2017**, *9*, e401.

(16) Wang, K.; Gunawan, O.; Todorov, T.; Shin, B.; Chey, S. J.; Bojarczuk, N. A.; Mitzi, D.; Guha, S. Thermally Evaporated Cu₂ZnSnS₄ Solar Cells. *Appl. Phys. Lett.* **2010**, *97*, No. 143508.

(17) Scragg, J. J.; Kubart, T.; Wätjen, J. T.; Ericson, T.; Linnarsson, M. K.; Platzer-Björkman, C. Effects of Back Contact Instability on Cu₂ZnSnS₄ Devices and Processes. *Chem. Mater.* **2013**, *25*, 3162–3171.

(18) López-Marino, S.; Placidi, M.; Pérez-Tomás, A.; Llobet, J.; Izquierdo-Roca, V.; Fontané, X.; Fairbrother, A.; Espindola-Rodríguez, M.; Sylla, D.; Pérez-Rodríguez, A.; Saucedo, E. Inhibiting the Absorber/Mo-Back Contact Decomposition Reaction in Cu₂ZnSnSe₄ Solar Cells: The Role of a ZnO Intermediate Nanolayer. *J. Mater. Chem. A* **2013**, *1*, 8338–8343.

(19) Li, W.; Chen, J.; Cui, H.; Liu, F.; Hao, X. Inhibiting MoS₂ Formation by Introducing a ZnO Intermediate Layer for Cu₂ZnSnS₄ Solar Cells. *Mater. Lett.* **2014**, *130*, 87–90.

(20) Liu, F.; Sun, K.; Li, W.; Yan, C.; Cui, H.; Jiang, L.; Hao, X.; Green, M. A. Enhancing the Cu₂ZnSnS₄ Solar Cell Efficiency by Back Contact Modification: Inserting a Thin TiB₂ Intermediate Layer at Cu₂ZnSnS₄/Mo Interface. *Appl. Phys. Lett.* **2014**, *104*, No. 051105.

(21) Qi, Y. F.; Kou, D. X.; Zhou, W. H.; Zhou, Z. J.; Tian, Q. W.; Meng, Y. N.; Liu, X. S.; Du, Z. L.; Wu, S. X. Engineering of Interface Band Bending and Defects Elimination via a Ag-Graded Active Layer for Efficient (Cu,Ag)₂ZnSn(S,Se)₄ Solar Cells. *Energy Environ. Sci.* **2017**, *10*, 2401–2410.

(22) Zhao, J. H.; Wang, A. H.; Green, M. A. 24.5% Efficiency Silicon PERT Cells on MCZ Substrates and 24.7% Efficiency PERL Cells on FZ Substrates. *Prog. Photovoltaics: Res. Appl.* **1999**, *7*, 471–474.

(23) Wang, A.; Zhao, J.; Green, M. A. 24% Efficient Silicon Solar Cells. *Appl. Phys. Lett.* **1990**, *57*, 602–604.

(24) Tarrant, D.; Ermer, J. In *I-III-VI₂ Multinary Solar Cells Based on CuInSe*, Multinary Solar Cells Based on CuInSe. Conference Record of the Twenty Third IEEE Photovoltaic Specialists Conference-1993; IEEE, 1993; pp 372–378.

(25) Singh, K. J.; Sarkar, S. K. Highly Efficient ARC Less InGaP/GaAs DJ Solar Cell Numerical Modeling Using Optimized InAlGaP BSF Layers. *Opt. Quant. Electron.* **2012**, *43*, 1–21.

(26) Green, M. A.; Blakers, A. W.; Zhao, J. H.; Milne, A. M.; Wang, A.; Dai, X. Characterization of 23-Percent Efficient Silicon Solar Cells. *IEEE Trans. Electron. Dev.* **1990**, *37*, 331–336.

(27) Schneiderlöchner, E.; Preu, R.; Lüdemann, R.; Glunz, S. W. Laser-Fired Rear Contacts for Crystalline Silicon Solar Cells. *Prog. Photovoltaics: Res. Appl.* **2002**, *10*, 29–34.

(28) Omrani, M. K.; Mimbashi, M.; Memarian, N.; Kim, D.-H. Improve the Performance of CZTSSe Solar Cells by Applying a SnS BSF layer. *Solid State Electron.* **2018**, *141*, 50–57.

- (29) Khattak, Y. H.; Baig, F.; Toura, H.; Ullah, S.; Mari, B.; Beg, S.; Ullah, H. Effect of CZTSe BSF and Minority Carrier Life Time on the Efficiency Enhancement of CZTS Kesterite Solar Cell. *Curr. Appl. Phys.* **2018**, *18*, 633–641.
- (30) Bär, M.; Nishiwaki, S.; Weinhardt, L.; Pookpanratana, S.; Shafarman, W. N.; Heske, C. Electronic Level Alignment at the Deeply Buried Absorber/Mo Interface in Chalcopyrite-Based Thin Film Solar Cells. *Appl. Phys. Lett.* **2008**, *93*, No. 042110.
- (31) Yang, J.; Wang, C.; Ju, H.; Sun, Y.; Xing, S.; Zhu, J.; Yang, Q. Integrated Quasiplane Heterostructures of MoSe₂/Bi₂Se₃ Hexagonal Nanosheets: Synergetic Electrocatalytic Water Splitting and Enhanced Supercapacitor Performance. *Adv. Funct. Mater.* **2017**, *27*, No. 1703864.
- (32) Song, Y.; Yao, B.; Li, Y.; Ding, Z.; Sun, H.; Zhang, Z.; Zhang, L.; Zhao, H. Self-Organized Back Surface Field to Improve the Performance of Cu₂ZnSn(S,Se)₄ Solar Cells by Applying P-Type MoSe₂:Nb to the Back Electrode Interface. *ACS Appl. Mater. Interfaces* **2019**, *11*, 31851–31859.
- (33) Shannon, R. D. Revised Effective Ionic Radii and Systematic Studies of Interatomic Distances in Halides and Chalcogenides. *Acta Crystallogr., Sect. A: Cryst. Phys., Diffraction, Theor. Gen. Crystallogr.* **1976**, *32*, 751–767.
- (34) Chen, S. Y.; Gong, X. G.; Walsh, A.; Wei, S. H. Defect Physics of the Kesterite Thin-Film Solar Cell Absorber Cu₂ZnSnS₄. *Appl. Phys. Lett.* **2010**, *96*, No. 021902.
- (35) Redinger, A.; Hönes, K.; Fontané, X.; Izquierdo-Roca, V.; Saucedo, E.; Valle, N.; Pérez-Rodríguez, A.; Siebentritt, S. Detection of a ZnSe Secondary Phase in Coevaporated Thin Films. *Appl. Phys. Lett.* **2011**, *98*, No. 101907.
- (36) Zhang, R.; Szczepaniak, S. M.; Carter, N. J.; Handwerker, C. A.; Agrawal, R. A Versatile Solution Route to Efficient Cu₂ZnSn(S,Se)₄ Thin-Film Solar Cells. *Chem. Mater.* **2015**, *27*, 2114–2120.
- (37) He, J.; Sun, L.; Chen, S.; Chen, Y.; Yang, P.; Chu, J. Composition Dependence of Structure and Optical Properties of Cu₂ZnSn(S,Se)₄ Solid Solutions: An Experimental Study. *J. Alloy Compd.* **2012**, *511*, 129–132.
- (38) Dimitrievska, M.; Giraldo, S.; Pistor, P.; Saucedo, E.; Pérez-Rodríguez, A.; Izquierdo-Roca, V. Raman Scattering Analysis of the Surface Chemistry of Kesterites: Impact of Post-Deposition Annealing and Cu/Zn Reordering on Solar Cell Performance. *Sol. Energy Mater. Sol. C* **2016**, *157*, 462–467.
- (39) Dimitrievska, M.; Fairbrother, A.; Saucedo, E.; Perez-Rodriguez, A.; Izquierdo-Roca, V. Influence of Compositionally Induced Defects on the Vibrational Properties of Device Grade Cu₂ZnSnSe₄ Absorbers for Kesterite Based Solar Cells. *Appl. Phys. Lett.* **2015**, *106*, No. 073903.
- (40) Dimitrievska, M.; Fairbrother, A.; Saucedo, E.; Pérez-Rodríguez, A.; Izquierdo-Roca, V. Secondary Phase and Cu Substitutional Defect Dynamics in Kesterite Solar Cells: Impact on Optoelectronic Properties. *Sol. Energy Mater. Sol. C* **2016**, *149*, 304–309.
- (41) Márquez, J.; Neuschitzer, M.; Dimitrievska, M.; Gunder, R.; Haass, S.; Werner, M.; Romanyuk, Y. E.; Schorr, S.; Pearsall, N. M.; Forbes, I. Systematic Compositional Changes and Their Influence on Lattice and Optoelectronic Properties of Cu₂ZnSnSe₄ Kesterite Solar Cells. *Sol. Energy Mater. Sol. C* **2016**, *144*, 579–585.
- (42) Tao, J.; Zhang, K.; Zhang, C.; Chen, L.; Cao, H.; Liu, J.; Jiang, J.; Sun, L.; Yang, P.; Chu, J. A Sputtered CdS Buffer Layer for Co-Electrodeposited Cu₂ZnSnS₄ Solar Cells with 6.6% Efficiency. *Chem. Commun.* **2015**, *51*, 10337–10340.
- (43) Gabor, A. M.; Tuttle, J. R.; Albin, D. S.; Contreras, M. A.; Noufi, R.; Hermann, A. M. High-Efficiency CuIn_xGa_{1-x}Se₂ Solar Cells Made from (In_xGa_{1-x})₂Se₃ Precursor Films. *Appl. Phys. Lett.* **1994**, *65*, 198–200.
- (44) Klenk, R.; Walter, T.; Schock, H. W.; Cuhen, D. A Model for the Successful Growth of Polycrystalline Films of CuInSe by Multisource Physical Vacuum Evaporation. *Adv. Mater.* **1993**, *5*, 114–119.
- (45) Tanaka, K.; Fukui, Y.; Moritake, N.; Uchiki, H. Chemical Composition Dependence of Morphological and Optical Properties of Cu₂ZnSnS₄ Thin Films Deposited by Sol–Gel Sulfurization and Cu₂ZnSnS₄ Thin Film Solar Cell Efficiency. *Sol. Energy Mater. Sol. C* **2011**, *95*, 838–842.
- (46) Yan, C.; Chen, J.; Liu, F.; Song, N.; Cui, H.; Ng, B. K.; Stride, J. A.; Hao, X. Kesterite Cu₂ZnSnS₄ Solar Cell from Sputtered Zn/(Cu & Sn) Metal Stack Precursors. *J. Alloy Compd.* **2014**, *610*, 486–491.
- (47) Scragg, J. J.; Ericson, T.; Kubart, T.; Edoff, M.; Platzer-Björkman, C. Chemical Insights into the Instability of Cu₂ZnSnS₄ Films During Annealing. *Chem. Mater.* **2011**, *23*, 4625–4633.
- (48) Su, Z.; Tan, J. M. R.; Li, X.; Zeng, X.; Batabyal, S. K.; Wong, L. H. Cation Substitution of Solution-Processed Cu₂ZnSnS₄ Thin Film Solar Cell with over 9% Efficiency. *Adv. Energy Mater.* **2015**, *5*, No. 1500682.
- (49) Godlewski, M. P.; Baraona, C. R., Jr; H, W. B. Low-High Junction Theory Applied to Solar Cells. *Sol. Cells* **1990**, *29*, 131–150.
- (50) Mandelkorn, J.; John, H.; Lamneck, J. A New Electric Field Effect in Silicon Solar Cells. *J. Appl. Phys.* **1973**, *44*, 4785–4787.
- (51) Cummertow, R. L. Use of Silicon p-n Junctions for Converting Solar Energy to Electrical Energy. *Phys. Rev.* **1954**, *95*, 561–562.
- (52) Luque, A.; Hegedus, S. *Handbook of Photovoltaic Science and Engineering*; John Wiley & Sons, 2002.
- (53) Virtuani, A.; Lotter, E.; Powalla, M. Performance of Cu(In,Ga)Se₂ Solar Cells under Low Irradiance. *Thin Solid Films* **2003**, *431-432*, 443–447.
- (54) van Lare, C.; Yin, G. C.; Polman, A.; Schmid, M. Light Coupling and Trapping in Ultrathin Cu(In,Ga)Se₂ Solar Cells Using Dielectric Scattering Patterns. *ACS Nano* **2015**, *9*, 9603–9613.
- (55) Haug, F. J.; Söderström, K.; Naqvi, A.; Ballif, C. Resonances and Absorption Enhancement in Thin Film Silicon Solar Cells with Periodic Interface Texture. *J. Appl. Phys.* **2011**, *109*, No. 084516.
- (56) Huang, L.; Wei, S.; Pan, D. Phase-Separation-Induced Crystal Growth for Large-Grained Cu₂ZnSn(S,Se)₄ Thin Film. *ACS Appl. Mater. Interfaces* **2018**, *10*, 35069–35078.
- (57) Lin, Y.; Ikeda, S.; Septina, W.; Kawasaki, Y.; Harada, T.; Matsumura, M. Mechanistic Aspects of Preheating Effects of Electrodeposited Metallic Precursors on Structural And Photovoltaic Properties of Cu₂ZnSnS₄ Thin Films. *Sol. Energy Mater. Sol. C* **2014**, *120*, 218–225.
- (58) Sun, K.; Liu, F.; Yan, C.; Zhou, F.; Huang, J.; Shen, Y.; Liu, R.; Hao, X. Influence of Sodium Incorporation on Kesterite Cu₂ZnSnS₄ Solar Cells Fabricated on Stainless Steel Substrates. *Sol. Energy Mater. Sol. C* **2016**, *157*, 565–571.
- (59) Sun, K.; Yan, C.; Liu, F.; Hao, X. In Towards 9% Sulfide CZTS Solar Cells Fabricated by a Sol-Gel Process, 2018 IEEE 7th World Conference on Photovoltaic Energy Conversion (WCPEC) (A Joint Conference of 45th IEEE PVSC, 28th PVSEC & 34th EU PVSEC); IEEE, 2018; pp 0856–0858.
- (60) Yang, K.-J.; Son, D.-H.; Sung, S.-J.; Sim, J.-H.; Kim, Y.-I.; Park, S.-N.; Jeon, D.-H.; Kim, J.; Hwang, D.-K.; Jeon, C.-W.; Nam, D.; Cheong, H.; Kang, J.-K.; Kim, D.-H. A Band-Gap-Graded CZTS Solar Cell with 12.3% Efficiency. *J. Mater. Chem. A* **2016**, *4*, 10151–10158.
- (61) Gao, S.; Zhang, Y.; Ao, J.; Lin, S.; Zhang, Z.; Li, X.; Wang, D.; Zhou, Z.; Sun, G.; Liu, F.; Sun, Y. Tailoring Mo(S,Se)₂ Structure for High Efficient Cu₂ZnSn(S,Se)₄ Solar Cells. *Sol. Energy Mater. Sol. C* **2018**, *176*, 302–309.
- (62) Lopez-Marino, S.; Espíndola-Rodríguez, M.; Sánchez, Y.; Alcobé, X.; Oliva, F.; Xie, H.; Neuschitzer, M.; Giraldo, S.; Placidi, M.; Caballero, R.; Izquierdo-Roca, V.; Pérez-Rodríguez, A.; Saucedo, E. The Importance of Back Contact Modification in Cu₂ZnSnSe₄ Solar Cells: The Role of a Thin MoO₂ Layer. *Nano Energy* **2016**, *26*, 708–721.
- (63) Siebentritt, S.; Rey, G.; Finger, A.; Regesch, D.; Sessler, J.; Weiss, T. P.; Bertram, T. What is the Band Gap of Kesterite? *Sol. Energy Mater. Sol. C* **2016**, *158*, 126–129.
- (64) Mendis, B. G.; Taylor, A. A.; Guennou, M.; Berg, D. M.; Arasimowicz, M.; Ahmed, S.; Deligianni, H.; Dale, P. J. Nanometre-

Scale Optical Property Fluctuations in $\text{Cu}_2\text{ZnSnS}_4$ Revealed by Low Temperature Cathodoluminescence. *Sol. Energy Mater. Sol. C* **2018**, *174*, 65–76.

(65) Gao, S.; Zhang, Y.; Ao, J.; Li, X.; Qiao, S.; Wang, Y.; Lin, S.; Zhang, Z.; Wang, D.; Zhou, Z.; Sun, G.; Wang, S.; Sun, Y. Insight into the Role of Post-Annealing in Air for High Efficient $\text{Cu}_2\text{ZnSn}(\text{S},\text{Se})_4$ Solar Cells. *Sol. Energy Mater. Sol. C* **2018**, *182*, 228–236.